Journal of Alloys and Compounds 511 (2012) 107–114

Contents lists available at SciVerse ScienceDirect

Journal of Alloys and Compounds

journal homepage: www.elsevier.com/locate/jallcom

Structural, magnetic and electrical properties of Al^{3+} substituted Ni–Zn ferrite nanoparticles

Mohd. Hashim[a,*], Alimuddin[a], Shalendra Kumar[b], Sikander Ali[a], B.H. Koo[b], H. Chung[c], Ravi Kumar[d]

[a] Department of Applied Physics, Aligarh Muslim University, Aligarh 202002, India
[b] School of Nano & Advanced Materials Engineering, Changwon National University, 9 Sarim dong, Changwon 641-773, Republic of Korea
[c] Department of Precision & Mechanical Engineering and BK21 Eco-Friendly Heat & Cooling Energy Mechanical Research Team, Gyeongsang National University, Tongyeong 650-160, Republic of Korea
[d] Centre for Material Science and Engineering, National Institute of Technology, Hamirpur, HP, India

ARTICLE INFO

Article history:
Received 27 July 2011
Received in revised form 26 August 2011
Accepted 29 August 2011
Available online 10 September 2011

Keywords:
Ferrites
Nanoparticles
Dielectric constant
Loss tangent
SEM
Magnetism

ABSTRACT

Nanocrystalline ferrite materials having the general formula $Ni_{0.7}Zn_{0.3}Fe_{2-x}Al_xO_4$ ($0.0 \le x \le 0.5$) have been synthesized by citrate-gel auto combustion method and characterized using X-ray diffraction (XRD), energy dispersive X-ray (EDX), field emission scanning electron microscopy (FE-SEM), dc magnetization, dielectric and impedance spectroscopy measurements. XRD studies confirm that all the samples show single phase cubic spinel structure. The crystallite size of $Ni_{0.7}Zn_{0.3}Fe_{2-x}Al_xO_4$ ($0.0 \le x \le 0.5$) nanoparticles calculated using the Debye–Scherrer formula was found in the range of 13–17 nm. The value of lattice parameter '*a*' is found to decrease with increasing Al^{3+} content. EDX patterns confirm the compositional formation of the synthesized samples. FE-SEM micrographs show that all the samples have nano-crystalline behavior and particles show spherical shape. The variation of dielectric properties ε',ε'', and $\tan\delta$ with frequency shows the dispersion behavior which is explained in the light of Maxwell–Wagner type of interfacial polarization in accordance with the Koop's phenomenological theory. The dc magnetization studies infer that magnetic moment of $Ni_{0.7}Zn_{0.3}Fe_{2-x}Al_xO_4$ ($0.0 \le x \le 0.5$) nanoparticles was found to decrease with Al doping. Impedance spectroscopy techniques have been used to investigate the effect of grain and grain boundary on the electrical properties of the synthesized compounds.

1. Introduction

During the last few decades, ferrites have achieved a primary position of economic and engineering importance within the family of magnetic materials because of their excellent physical properties. Practically all TV sets have ferrite cores in the fly back transformers, while portable radios make use of a pencil of ferrite as an antenna core. Long distance carrier telephone circuits are employing ferrite cores in high quality filter coils and transformers. Various physical properties of nanocrystalline ferrites are highly influenced by distribution of cations among the sub lattices, nature of grain (shape, size, and orientation), grain boundaries, voids, in homogeneities, surface layers, contacts, etc. [1–3]. The information about the associated physical parameters of the microstructural components is important; since, the overall property of the materials is determined by these components. Progresses in the use and development of new ferrites have been rapid as compared to other areas of research [4–9]. One important characteristic of ferrites is their high values of resistivity and low eddy current losses [10–13], which make them ideal for high frequency applications. For microwave applications, the dielectric properties such as dielectric constant and dielectric loss are very important as the dielectric constant affects the thickness of microwave absorbing layer and the dielectric loss factor ($\tan\delta$) of a material determines dissipation of the electrical energy. This dissipation may be due to electrical conduction, dielectric relaxation, dielectric resonance and loss from non-linear processes. Recently, Kumar et al. have reported that ferrites also behave like multiferroics [14]. The major interest in the synthesis of uniform magnetic nanocrystals with controllable size and their physical properties has stimulated a search for general schemes to prepare high-quality magnetic nanocrystals of varying compositions. There are many researchers who studied the magnetic properties of nickel–zinc ferrites but for the nonmagnetic properties such as electrical conductivity and dielectric properties are seldom reported.

In this work, chemical-route technique has been chosen for the synthesis of $Ni_{0.7}Zn_{0.3}Fe_{2-x}Al_xO_4$ ($0.0 \le x \le 0.5$) nanoparticles. Various techniques such as; XRD, FE-SEM, dc magnetization, dielectric and impedance spectroscopy measurements have been used to study their structural, magnetic and electrical properties.

* Corresponding author. Tel.: +91 9359380185.
E-mail address: md.hashim09@gmail.com (Mohd. Hashim).

0925-8388/$ – see front matter © 2011 Elsevier B.V. All rights reserved.
doi:10.1016/j.jallcom.2011.08.096

Structural studies infer that all the samples have single phase cubic spinel structure and lattice parameters decreases with increase in Al content. The saturation magnetization calculated from magnetic hysteresis loop was found to decrease with increase in Al doping. FE-SEM micrographs show the nanocrystalline behavior of the samples. Evaluation of electrical conductivity reveals a wealth of information as regards the usefulness of these materials for various applications. Moreover the study of dielectric sheds light on the behavior of charge carriers under the ac field, their mobility and the mechanism of conduction.

2. Experimental

Nanoparticles of $Ni_{0.7}Zn_{0.3}Al_xFe_{2-x}O_4$ ($0.0 \le x \le 0.5$) ferrite were prepared by using citrate gel auto combustion method. The chemical reagents used in this work were Ni $(NO_3)_2 6H_2O$, Zn $(NO_3)_2 \cdot 6H_2O$, Fe $(NO_3)_3 \cdot 9H_2O$ and Al $(NO_3)_3 \cdot 9H_2O$ as starting materials. All the chemicals were of analytical grade. We use citric acid $C(OH)(COOH)(CH_2 \cdot COOH)_2 \cdot H_2O$ (M.W.210.14) in this method because citric acid is a weak acid and has three carboxylic and one hydroxyl group for coordinating metal ions and therefore enhances the homogeneous mixing. Citric acid helps for the homogenous distribution and segregation of the metal ions. During water dehydration, it suppresses the precipitation of metal nitrates because it has electronegative oxygen atoms interacting with electropositive metal ions. Therefore, at a relative low temperature the precursors can form a homogenous single phase. The ammonia is used to adjust the pH for improving the complication, gel formation and also to improve the solubility of metal ions. Metal nitrates taken in the required stoichiometric ratio were dissolved in a minimum amount of distilled water and mixed together. The mixed metal nitrate solution was then added to the citric acid solution in 1:1 molar ratio. The pH value of the clear solution thus obtained was unity. Analytical grade liquor ammonia (30%) was then added drop-wise under constant stirring in order to reach the pH of the solution up to 6. The resulting solution was continuously heated on the magnetic stirrer at 70 °C in order to allow gel formation. The gel so formed is kept in an air oven at 100 °C for 36 h in order to remove the adsorbed water [15]. During this process the gel swells into a fluffy mass, which eventually breaks into brittle flakes. This precursor powder was then calcined at 600 °C for 8 h to obtain final product. The rate of heating and cooling was maintained 10°/min. The resultant powders were grind into fine particles using an agate mortar and pestle. The structural characterization of all samples was carried out by Rigaku X-ray diffractometer (Rigaku Miniflex II) using the CuKα radiation (wavelength λ = 1.5406 Å). Field emission scanning electron microscopy (FE-SEM) images were obtained using a TESCAN, MIRA II LMH microscope. The composition was determined by energy dispersive X-ray spectroscopy (EDX, Inca Oxford, attached to the FE-SEM). For the FE-SEM and EDX measurements, the nanoparticles of $Ni_{0.7}Zn_{0.3}Fe_{2-x}Al_xO_4$ ($0.0 \le x \le 0.5$) ferrite were dispersed homogeneously in ethanol using ultrasonic treatment. A minute drop of nanoparticles solution was cast on to a glass slide followed by subsequently drying in air before transfer it into the microscope. The dielectric and impedance spectroscopy measurements were carried out using LCR HI-Tester (HIOKI3532-50) at room temperature in the frequency range from 42 Hz to 5 MHz. Shielded test leads were used for the electrical connections from the LCR meter to the sample in order to avoid any parasitic impedance. The samples were made in the form of circular pellets. Before starting the measurements the samples were heated at 100 °C for 1 h, so as to homogenize the charge carriers and to remove the moisture content therein. The surface of the disks was coated on adjacent faces with silver paste, thereby forming parallel plate capacitor geometry.

The value of real dielectric constant (ε') has been calculated using the following relation:

$$\varepsilon' = \frac{c_p \times t}{\varepsilon_0 A} \tag{1}$$

where $\varepsilon_0 = 8.85 \times 10^{-14}$ F/cm, known as permittivity of the free space, t is the thickness of pellets, A is the cross sectional area of the flat surface of the pellets and c_p is the capacitance of the pellet in (F). The imaginary dielectric constant has been calculated by the relation:

$$\varepsilon'' = \varepsilon' \tan \delta \tag{2}$$

where $\tan\delta$ is the dielectric loss tangent which is proportional to the 'loss' of energy from the applied field into the sample (in fact this energy is dissipated into heat) and therefore denoted as dielectric loss.

The loss tangent has been calculated from the following relation:

$$\tan \delta = \frac{1}{2\pi f \varepsilon_0 \varepsilon' \rho} \tag{3}$$

here f is the frequency of the applied field and ρ is the resistivity. The magnetic measurements were performed using Quantum design physical properties measurement system (PPMS 6000).

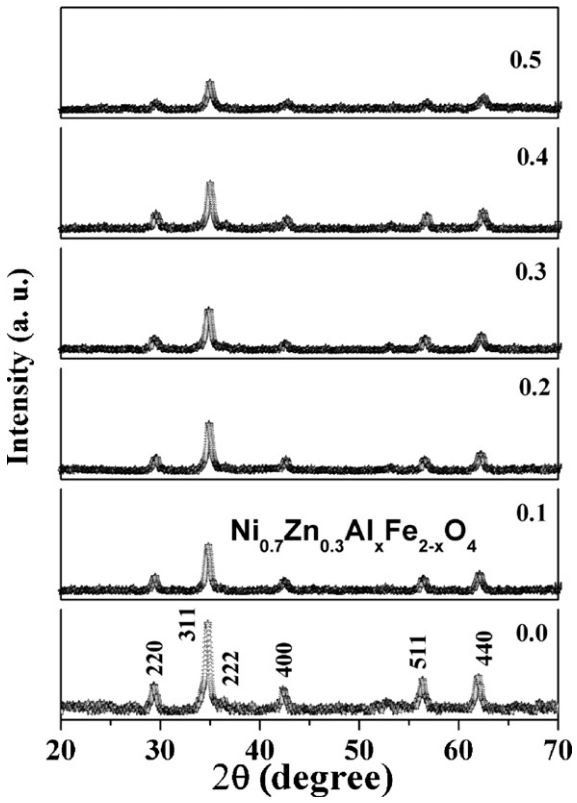

Fig. 1. X-ray diffraction pattern of $Ni_{0.7}Zn_{0.3}Al_xFe_{2-x}O_4$ ($0.0 \le x \le 0.5$) ferrite nanoparticles.

3. Results and discussion

Fig. 1 highlights the XRD patterns of $Ni_{0.7}Zn_{0.3}Al_xFe_{2-x}O_4$ ($0.0 \le x \le 0.5$) ferrite nanoparticles. It can be clearly seen from Fig. 1 that all samples exhibit single phase cubic spinel structure and exclude presence of any undesirable secondary phase. Moreover, the broadening of the XRD peaks indicate that $Ni_{0.7}Zn_{0.3}Al_xFe_{2-x}O_4$ ($0.0 \le x \le 0.5$) ferrite have nano-crystalline behavior. The crystallite size $Ni_{0.7}Zn_{0.3}Al_xFe_{2-x}O_4$ ($0.0 \le x \le 0.5$) ferrite nanoparticles was calculated from the most intense peak (3 1 1) of XRD data using Debye Scherrer formalism:

$$t = \frac{0.9\lambda}{\beta \cos \theta} \tag{4}$$

where $\beta = (\beta_M^2 - \beta_i^2)^{1/2}$. Here λ is X-ray wavelength (1.54 Å for Cu K_α), β_M and β_i are the measured and instrumental broadening in radians respectively and θ is the Bragg's angle in degrees. The calculated value of particle size was found to increase from 13 to 17 nm (see Table 1) with Al doping, which implies that Al doping favor the particle growth. The lattice parameters calculated using Powder-X software was found to decrease from 8.516 Å to 8.385 Å (see Table 1) with increase in Al^{3+} content. The values of the lattice parameters observed in $Ni_{0.7}Zn_{0.3}Al_xFe_{2-x}O_4$ ($0.0 \le x \le 0.5$) ferrite nanoparticles are in good agreement with the reported value for cubic spinel ferrites [16,17]. The decrease in lattice parameters with increase in Al^{3+} doping can be explained on the basis of difference in the ionic radii of Fe and Al ions, since, the ionic radius of Al^{3+} ion (0.57 Å) is smaller than that of Fe^{3+} ion (0.67 Å). The variation in the X-ray density (theoretical density) and apparent density (experimental density) with Al^{3+} ion concentration is shown in Table 1. It is clear from the table that the X-ray density decreases with the increase of Al^{3+} ion concentrations. This can be explained on the basis of the fact that the density and the atomic weight of the Al atoms

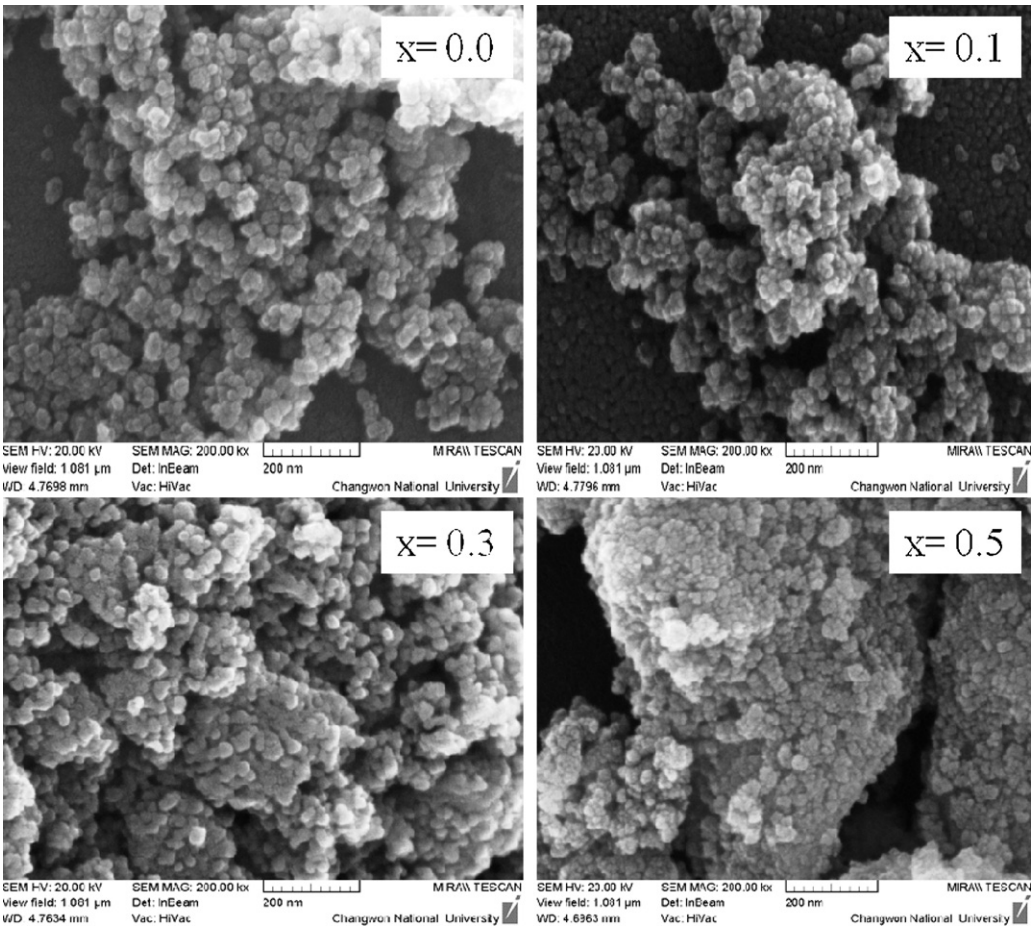

Fig. 2. Field emission scanning electron micrographs of $Ni_{0.7}Zn_{0.3}Al_xFe_{2-x}O_4$ ($0.0 \le x \le 0.5$) ferrite nanoparticles.

(2.70 and 26.981 g/cm^3), which are less than that of Fe atoms (7.86 and 55.847 g/cm^3). The apparent density of the same composition reflects the same general behavior as that of the X-ray density. The X-ray density is higher than the apparent density. This may be due to the existence of pores in the sample, which depends upon the sintering conditions. Table 1 also shows the variation of the porosity of samples with composition. The porosity of the samples increases with composition; this may be due to the lower density of Al^{3+} ions. The increase in porosity is also explained on the basis of the crystallite size.

Fig. 2 shows the FE-SEM micrographs of $Ni_{0.7}Zn_{0.3}Al_xFe_{2-x}O_4$ ($0.0 \le x \le 0.5$) ferrite nanoparticles. It can be seen from the micrographs that all samples are composed of nano crystallite. Micrographs also show the uniform grain growth with Al substitution and a decrease in porosity. It is clear from the micrographs that all the samples have the spherical shape crystallite with agglomeration and highly dense clusters are found with increasing the doping concentration. The chemical compositions of $Ni_{0.7}Zn_{0.3}Al_xFe_{2-x}O_4$ ($0.0 \le x \le 0.5$) ferrite nanoparticles have been calculated by EDX. Fig. 3 shows the EDX pattern for the various compositions of $Ni_{0.7}Zn_{0.3}Al_xFe_{2-x}O_4$ ($0.0 \le x \le 0.5$) ferrite nanoparticles. The peaks of the elements Fe, Ni, Zn, Al and O were observed and have been assigned. Peaks other than Fe, Ni, Zn, Al and O are from the glass slide. Since for EDX measurements the nanoparticles of $Ni_{0.7}Zn_{0.3}Al_xFe_{2-x}O_4$ ($0.0 \le x \le 0.5$) ferrite were dispersed on glass slide. The calculated percentage of Ni/Zn value matches well with the amount of Ni/Zn used in the respective precursors. The EDX pattern confirmed the homogeneous mixing of the Ni, Zn, Fe, Al and O atoms in pure and doped ferrite samples. The observed composition is almost equal to that of the sample produced by stoichiometric calculations.

Fig. 4(a) and (b) shows the variation of real and imaginary part of the dielectric constant of $Ni_{0.7}Zn_{0.3}Al_xFe_{2-x}O_4$ ($0.0 \le x \le 0.5$) ferrite nanoparticles in the frequency range from 42 Hz to 5 MHz at room temperature. During the process of preparation of ferrites in polycrystalline form, the formation of grains with high

Table 1
Structural properties of $Ni_{0.7}Zn_{0.3}Al_xFe_{2-x}O_4$ ($0.0 \le x \le 0.5$) ferrite nanoparticles.

Composition	Lattice parameter (Å)	Density (g/cm^3)		Porosity (%)	Crystallite size (nm)
		(Dtho)	(Dexp)		
$x = 0.0$	8.516	3.707	2.755	25.68	17.090
$x = 0.1$	8.508	3.655	2.678	26.73	15.164
$x = 0.2$	8.472	3.639	2.625	27.86	15.808
$x = 0.3$	8.440	3.617	2.599	28.14	13.430
$x = 0.4$	8.406	3.596	2.573	28.73	15.795
$x = 0.5$	8.385	3.575	2.547	28.75	13.449

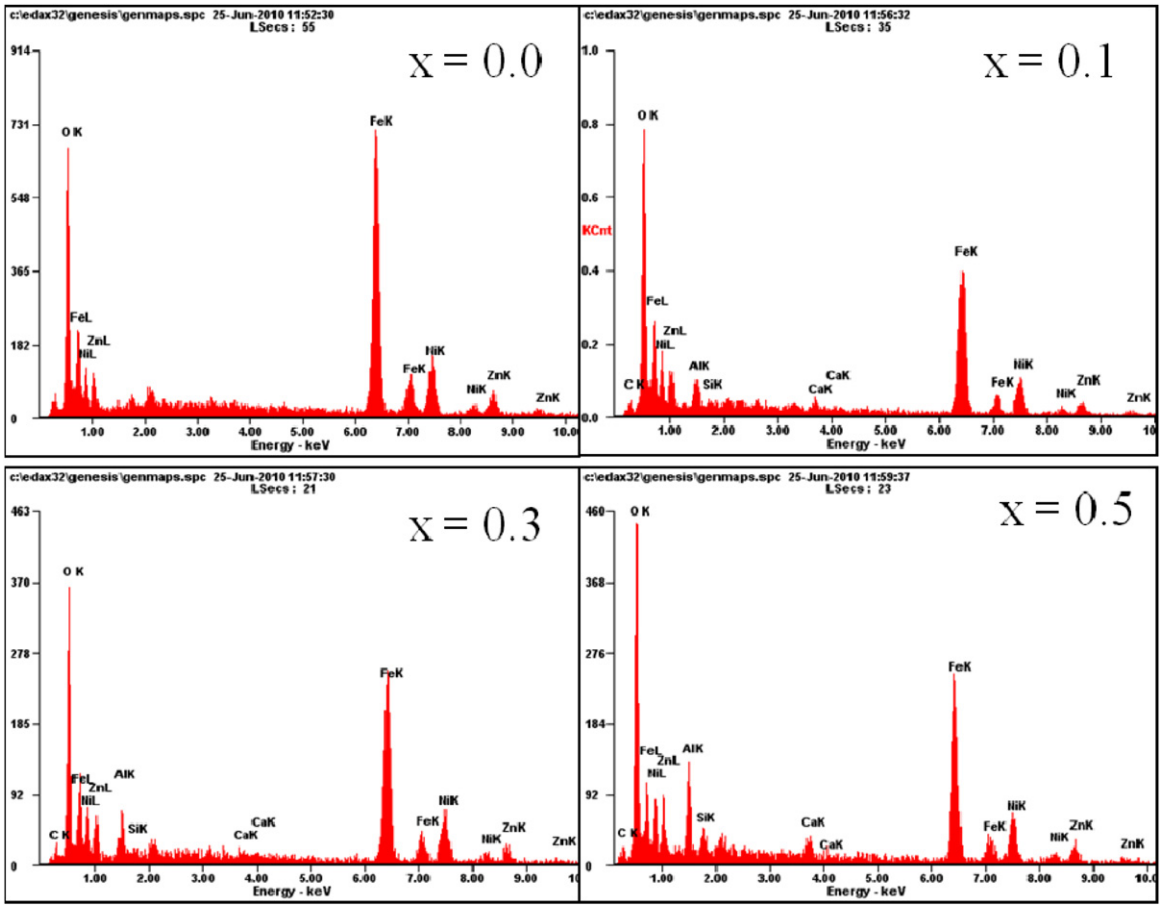

Fig. 3. EDX pattern of $Ni_{0.7}Zn_{0.3}Al_xFe_{2-x}O_4$ ($0.0 \le x \le 0.5$) ferrite nanoparticles.

conductivity takes place, these grains are separated by thin layers which exhibit poor conduction and thus they behave as heterogeneous dielectric materials. In addition to this, generation of Fe^{2+} ions from Fe^{3+} ions also occurs. Generally at low frequencies (in kHz region), the value of dielectric constant (ε) ranges approximately in the order of 10^4–10^6. Hence, ferrites are good dielectric materials. The value of both real and imaginary part of dielectric constant is much higher at lower frequencies. It decreases with the increase of frequency. At very high frequencies, its value becomes so small that it becomes independent of frequency as prescribed [18]. The variation in dielectric constant may be explained on the basis of space charge polarization which is produced due to the presence of higher conductivity phases (grains) in the insulating matrix (grain boundaries) of a dielectric produces localized accumulation of charge under the influence of an electric field as demonstrated [19]. The assembly of space charge carriers in a dielectric takes a finite time to line up their axes parallel to an alternating electric field. If the frequency of the field reversal increases, a point is reached where the space charge carriers cannot keep up with the field and the alternation of their direction lags behind that of the field as said [19]. Decreasing order of dielectric constant with increasing frequency can be explained on the basis of Maxwell and Wagner two layer model. According to this model [20,21], space charge polarization is because of inhomogeneous dielectric structure of the material. It is formed by large well conducting grains separated by thin poorly conducting intermediate grain boundaries. Rabinkin and Novikova [22] pointed out that polarization in ferrites is a similar process to that of conduction. The electron exchange between $Fe^{2+} \leftrightarrow Fe^{3+}$ results the local displacement of electrons in the direction of applied field that determines the polarization. Polarization decreases with the increase in value of frequency and then reaches a constant value. It is due to the fact that beyond a certain frequency of external field, the electron exchange between $Fe^{2+} \leftrightarrow Fe^{3+}$ cannot follow the alternating field. It is because of the predominance of species like Fe^{2+} ions, oxygen vacancies, grain boundary defects, interfacial dislocation pile ups, voids, etc. [21,23]. The decreasing trend in dielectric constant with the increase in frequency is natural due to the fact that any species contributing to polarizability is found lagging behind the applied field at higher frequencies [24].

The variation in dielectric loss with frequency is shown in Fig. 5. From the figure it is clear that dielectric loss shows the abnormal behavior for all the samples. The initial decrease of tan δ with increasing frequency can be explained on the basis of Koop's phenomenological theory of dielectrics. A maximum value of loss tangent at a certain frequency can be observed when (ε) has a minimum value, i.e., a minimum stored energy at that frequency. All the samples exhibit the Debye relaxation in the measured frequency range (42 Hz–5 MHz). The observed abnormal behavior of loss tangent with frequency can be explained in the light of Rezlescu model [25]. According to this model, a resonance peak (Debye relaxation) will occur when the hopping frequency of the charge exchange approximately matches to the frequency of the applied field, there is a slight shift in the maxima towards the higher frequency region. It is observed that height of the peak also varies with Al-doping. This peaking nature is observed when the jumping frequency of electrons between Fe^{2+} and Fe^{3+} becomes approximately equal to the frequency of the applied field. The shift of maxima towards the

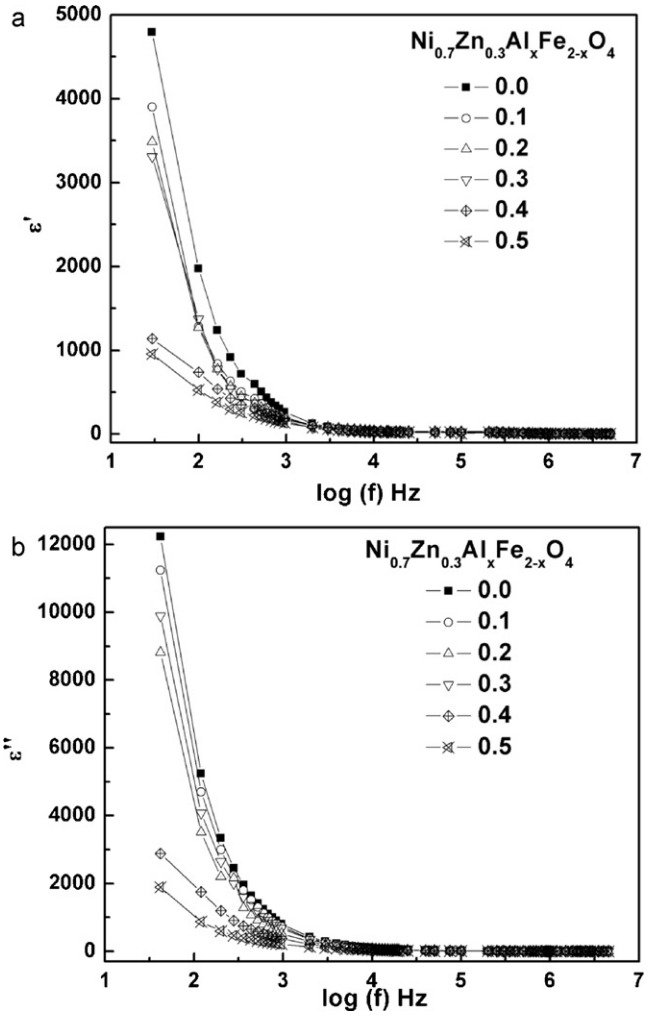

Fig. 4. (a) Variation of real part of dielectric constant as a function of frequency for $Ni_{0.7}Zn_{0.3}Al_xFe_{2-x}O_4$ ($0.0 \le x \le 0.5$) ferrite nanoparticles at room temperature. (b) Variation of imaginary part of dielectric constant as a function of frequency for $Ni_{0.7}Zn_{0.3}Al_xFe_{2-x}O_4$ ($0.0 \le x \le 0.5$) ferrite nanoparticles at room temperature.

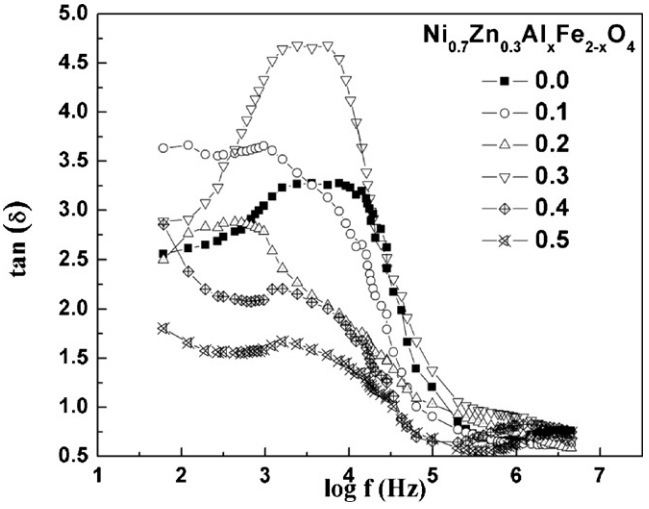

Fig. 5. Variation of dielectric loss as a function of frequency for $Ni_{0.7}Zn_{0.3}Al_xFe_{2-x}O_4$ ($0.0 \le x \le 0.5$) ferrite nanoparticles at room temperature.

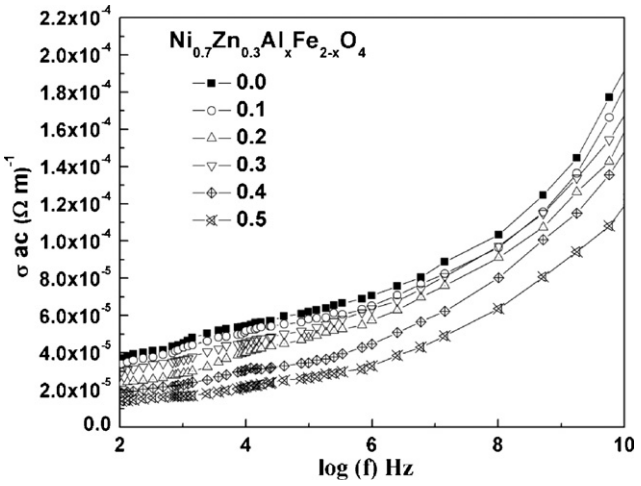

Fig. 6. Variation of ac conductivity with ln$f$ for $Ni_{0.7}Zn_{0.3}Al_xFe_{2-x}O_4$ ($0.0 \le x \le 0.5$) ferrite nanoparticles at room temperature.

higher frequency region with Al-doping indicates that the jumping probability increases. The increase in peak height with Al-doping is attributed to the decrease of resistivity arising due to the increase of Fe^{3+}/Fe^{2+} ion pairs available for the conduction process.

Fig. 6 shows the variation of ac conductivity as a function of frequency at room temperature. It is observed that all the samples show an increasing trend in the ac conductivity as the frequency increases, which is a general behavior of ferrites. The electrical conductivity in ferrites is mainly due to hopping of electrons between ions of the same element present in more than one valence state, distributed randomly over crystallographic equivalent lattice sites. Ferrites have cubic close packed oxygen lattice with the cation at octahedral (B) and tetrahedral (A) sites. The distance between two metal ions on B-sites is smaller (0.292 nm) than the distance between two metals ions on A-sites (0.357 nm), therefore, the hopping between A- and B-sites have very small probability compared with that at B-sites. The hopping between A–A sites does not exist, due to the fact that there are only Fe^{3+} ions at A-sites and any Fe^{2+} ions formed during sintering process preferentially occupy B-sites only [26]. The charges migrate under the influence of the applied field, contributing to the electrical response of the system. The conductivity is an increasing function of frequency in case of conduction by hopping and a decreasing function of frequency in case of band conduction [27].

The frequency dependence of ac conductivity is expressed as:

$$\sigma_{tot} = \sigma_o(T) + \sigma(\omega, T) \quad (5)$$

where the first term is dc conductivity due to band conduction and is frequency independent function. The second term is pure ac conductivity due to the hopping processes at the octahedral site and is frequency dependent function. The first term is predominant at low frequencies and at high temperature, while the second term is predominant at high frequencies and at low temperature.

The frequency dependence of the second term σ_{ac} can be written as empirical formula [28]:

$$\sigma_{ac} = A\omega^n \quad (6)$$

where A is a constant having the units of conductivity, σ is the real part of the conductivity, ω is angular frequency ($\omega = 2\pi f$), and "n" is an exponent. The frequency response of ac conductivity can be explained on the basis that at low frequencies where the conductivity is constant, the transport takes place on infinite paths. For a region of frequencies, where the conductivity increases strongly with frequency, the electrical transport phenomenon is dominated by contributions from hopping between

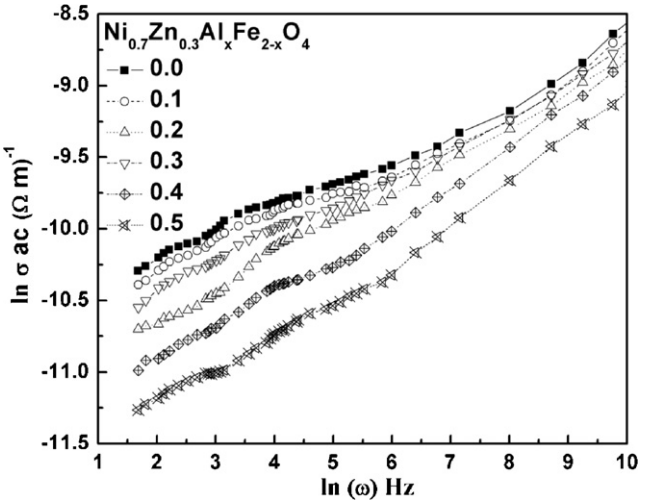

Fig. 7. Variation of ln ac conductivity with ln(ω) for $Ni_{0.7}Zn_{0.3}Al_xFe_{2-x}O_4$ ($0.0 \le x \le 0.5$) ferrite nanoparticles at room temperature.

infinite clusters. Finally, the region, where high frequency cut-off starts to play a role is encountered. The electrical conduction mechanism can be explained in terms of the electron-hopping model. In other words, the conduction mechanism is due to the electron hopping between two adjacent octahedral sites (B-sites), $Fe^{2+} \Leftrightarrow Fe^{3+}$ ions or $Ni^{2+} \Leftrightarrow Ni^{3+}$ in the spinel lattice of nanocrystalline $Ni_{0.7}Zn_{0.3}Fe_{2-x}Al_xO_4$ samples. Consequently, the increase in frequency enhances the rate of hopping between the charge carriers and hence increases the conduction process, or conductivity in the investigated samples. Further, at high frequencies, the resistivity remains invariant with frequency because of the fact that hopping frequency no longer follows the changes of external field beyond a certain frequency limit and thus lags behind it [29].

Fig. 7 shows the variation of $\ln\sigma$ versus $\ln\omega$ in the frequency range 42 Hz–5 MHz at room temperature. The composition $x = 0.0$, is found to have the maximum value of σ_{ac}. Following charge exchange mechanism is suggested for the mixed Ni–Zn ferrite:

$$Ni^{2+} + Fe^{3+} \leftrightarrow Ni^{3+} + Fe^{2+}$$

It is observed that σ_{ac} decreases as the Al content increases in the samples. The behavior can be explained on the basis that the Al

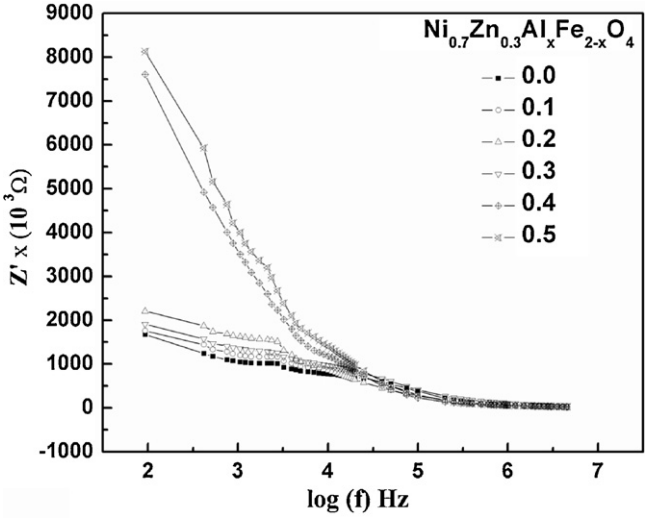

Fig. 8. Variation of real (Z') of impedance with frequency for $Ni_{0.7}Zn_{0.3}Al_xFe_{2-x}O_4$ ($0.0 \le x \le 0.5$) ferrite nanoparticles at room temperature.

Table 2
Impedance parameters of $Ni_{0.7}Zn_{0.3}Al_xFe_{2-x}O_4$ ($0.0 \le x \le 0.5$) ferrite nanoparticles at room temperature for grain.

Composition	R_g	C_g	τ_g
$x = 0.0$	99	2.4E−6	2E−2
$x = 0.1$	76	4.0E−6	3E−2
$x = 0.2$	108	2.6E−6	2E−2
$x = 0.3$	140	1.4E−6	2E−2
$x = 0.4$	154	9.6E−7	1E−2
$x = 0.5$	205	5.9E−7	1E−2

ions occupy the octahedral sites in the mixed Ni–Zn ferrite, depleting the Fe number present at the octahedral site. The doping of Al ions decreases the Fe number as well as isolates them which results decrease in the probability of charge hoping in the following mechanism:

$$Ni^{2+} + Fe^{3+} \leftrightarrow Ni^{3+} + Fe^{2+},\ Fe^{3+} \leftrightarrow Fe^{2+} + e^{-}$$

Bauerle [30,31], was the first to use the impedance spectroscopy technique in 1969 to separate bulk from interfacial properties in polycrystalline ceramics. In complex impedance diagrams (Nyquist or Cole–Cole plot), the imaginary part of the impedance is plotted against the real part of impedance. The response of an ideal parallel circuit of resistance R and capacitance C is a semicircle centred on the real axis. R is determined from the diameter of the semicircle, whereas C is calculated from the frequency of semicircle maximum. Impedance spectroscopy is ideal for investigating the electrical response of dielectric materials as a function of frequency. It is a powerful technique for unraveling the complexities of materials, whose properties and applications depend on the close control of structure, composition, ceramic texture, dopants (or defects) and dopant distribution, which functions by utilizing the different frequency dependencies of constituent components for their separation. The impedance analysis of a material is based on an idealized circuit model with discrete electrical components. The analysis is mainly accomplished by fitting the impedance data to an equivalent circuit, which is representative of the material under investigation. It has been among the most useful investigating techniques, since the impedance of grains can be separated from the other sources of impedance, namely grain boundaries and electrode effects [32,33].

Generally, two semicircles are observed in the Cole–Cole plot; first semicircle at low frequency represents the resistance of the grain boundary and second semicircle obtained at high frequency corresponds to the resistance of grain or bulk properties. The phenomenon is typically related to the existence of a distribution of relaxation time, which is according to the Cole–Cole type of distribution based on two-layer model, in which the resulting complex impedance is composed of two overlapping semicircles.

The complex impedance of a system at an applied frequency can be written as sum of the real and imaginary parts:

$$Z^*(\omega) = Z'(\omega) + iZ''(\omega) \tag{7}$$

where Z' and Z'' of the impedance can be written as

$$Z' = \frac{R_g}{(1+\omega_g C_g R_g)^2} + \frac{R_{gb}}{(1+\omega_{gb} C_{gb} R_{gb})^2} \tag{8}$$

$$Z'' = \frac{R_g^2}{1+(R_g\omega_g C_g)^2} + \frac{R_{gb}^2}{1+(R_{gb}\omega_{gb} C_{gb})^2} \tag{9}$$

where R_g and C_g represent the resistance and capacitance of the grain and R_{gb} and C_{gb} represent the corresponding terms for grain boundary, while ω_g and ω_{gb} are the frequencies at the peaks of the semicircles for grain and grain boundary respectively. The resistances are calculated from the circular arc intercepts on the Z' axis, while the capacitances are derived from the maximum height of the

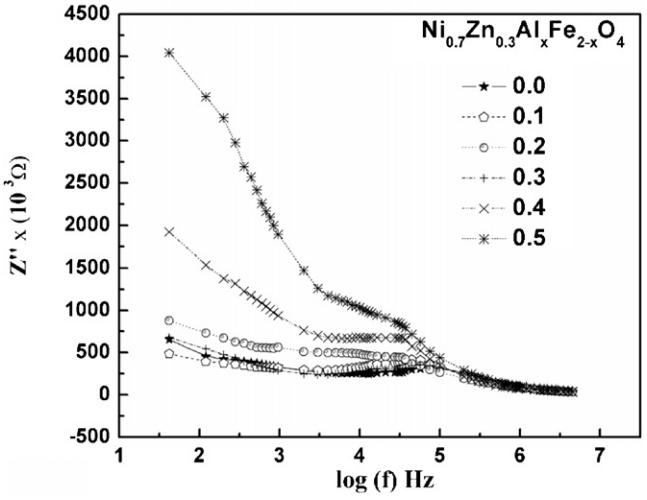

Fig. 9. Variation of imaginary part (Z'') of impedance with frequency for $Ni_{0.7}Zn_{0.3}Al_xFe_{2-x}O_4$ ($0.0 \le x \le 0.5$) ferrite nanoparticles at room temperature.

circular arcs. The maximum height in each semicircle is $Z' = -Z''$, therefore by using this condition and using relations (8) and (9), we can calculate the capacitances for grain and grain boundary by using the relations (10) and (11):

By using the above two relations the relaxation times for grain and grain boundary were calculated by relations (10) and (11)

$$\tau_g = \frac{1}{\omega_g} = C_g R_g \tag{10}$$

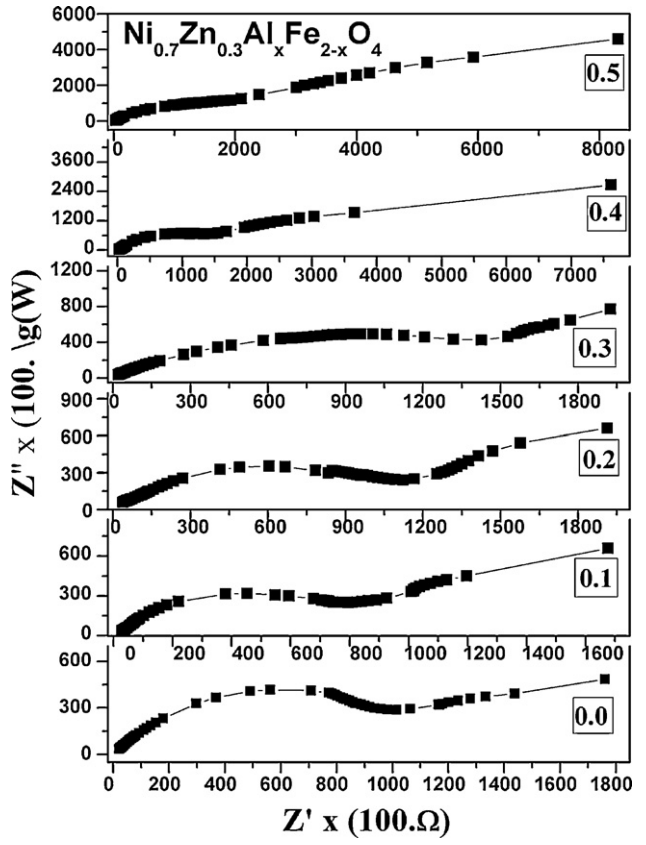

Fig. 10. Cole–Cole plot for $Ni_{0.7}Zn_{0.3}Al_xFe_{2-x}O_4$ ($0.0 \le x \le 0.5$) ferrite nanoparticles at room temperature.

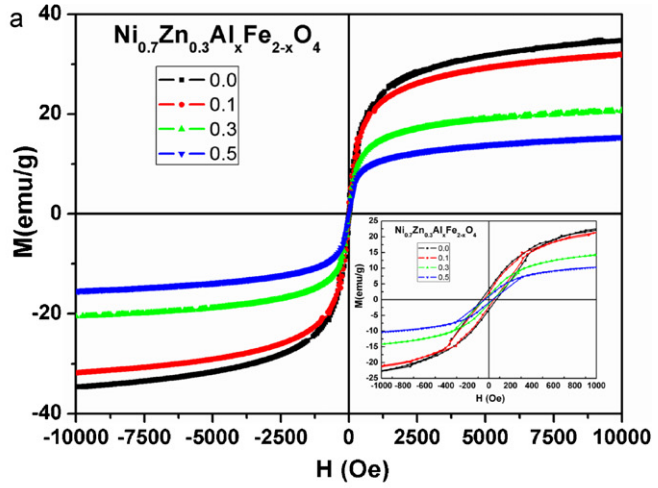

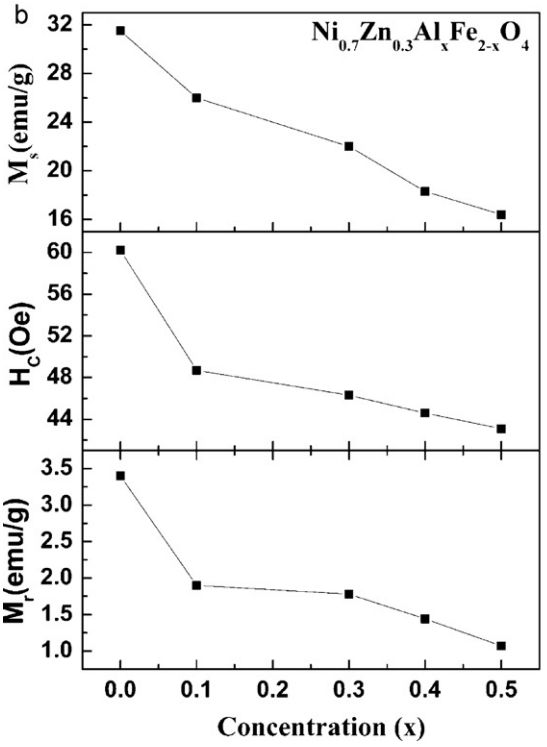

Fig. 11. (a) M–H curves for $Ni_{0.7}Zn_{0.3}Al_xFe_{2-x}O_4$ ($0.0 \le x \le 0.5$) ferrite nanoparticles at room temperature. Inset shows the expanded view of M–H curve at low field. (b) Saturation magnetization (M_s), coercive field (H_C) and remnant magnetization (M_r) as a function of Al doping.

$$\tau_{gb} = \frac{1}{\omega_{gb}} = C_{gb} R_{gb} \tag{11}$$

The various calculated electrical parameters are shown in Table 2. Fig. 8 represents the variation of real part of impedance as a function of frequency at room temperature. It can be seen that Z' decreases as the frequency gradually increases. The maximum value of Z' is observed for the composition $x = 0.5$. The higher value of the resistance means conductivity is lowered. Fig. 9 shows the variation of reactive part of the impedance with frequency for all the compositions at room temperature. It is seen that the Z'' decreases as the frequency increases and the composition $x = 0.5$ is having the maximum value of Z''. In order to distinguish the contribution from grain and grain boundary, complex impedance plots or Cole–Cole plots are obtained by plotting the real part

corresponding to the imaginary part. It is clear from Fig. 10 that all the samples show one full semicircle that is due to the conduction of the grain and one incomplete semicircle, which is due to the conduction of the grain boundary. This shows that the grain boundary resistance is out of measurement scale.

Fig. 11(a) represents magnetic hysteresis loops of $Ni_{0.7}Zn_{0.3}Al_xFe_{2-x}O_4$ ($0.0 \le x \le 0.5$) ferrite nanoparticles. It can be seen from the inset in Fig. 11(a) that all samples have ferrimagnetic ordering above room temperature. Fig. 11(b) shows the remnant magnetization (M_r) and coercive field (H_C) and saturation magnetization (M_s) as a function of Al doping. It is observed that the value of M_r and H_C was found to decrease from 3.4 to 1.07 emu/g and 60.2–43.1 Oe, respectively. The values of the saturation magnetization (M_s) calculated by plotting M versus $1/H$ curve and extrapolating the $1/H \to 0$, were found to decrease from 31.5 to 16.4 emu/g with increase in the Al doping. The decrease in the M_s value with doping of nonmagnetic ions are similar to the earlier reported results [34,35] and can be explained in the light of Neel's two sub-lattice model for ferrimagnetism. According to Neel's model the net magnetic moment of the system is the difference of the magnetic moment at A and B sub-lattice (i.e. magnetic moment at B sub-lattice – magnetic moment at A sub-lattice). Since the doping of Al^{3+} ions occupy the B sub-lattice which results decrease the magnetic moment of the system.

4. Conclusion

We have successfully synthesized $Ni_{0.7}Zn_{0.3}Al_xFe_{2-x}O_4$ ($0.0 \le x \le 0.5$) ferrite nanoparticles using chemical route. XRD results indicate that all samples have single phase cubic spinel structure. Lattice parameters and crystallite size have been found to decrease with Al doping. FE-SEM micrographs show that all particles have spherical shape nano-crystalline behavior. The real and imaginary part of the dielectric constant was found to decrease with frequency and explained in the light of electron hopping mechanism and space charge polarization discussed by Maxwell–Wagner model and Koop's phenomenological theory. The ac conductivity was found to increase with frequency and discussed in the light of electron hoping between Fe^{2+} and Fe^{3+} ions. The complex impedance measurements show two semicircles for all the samples, which shows that the resistive and the capacitive properties of the samples are associated with the grain and grain boundaries. Magnetic study infers that saturation magnetization, remnant magnetization and coercive field decreases with increase in Al doping which may be due to the dilution of the sub-lattice by nonmagnetic ions doping.

Acknowledgments

Grateful thanks are due to U.G.C., New Delhi, for financial support and Centre of Excellence in Material Science (Nanomaterials), Department of Applied Physics, Aligarh Muslim University, Aligarh, for providing facility for doing this work. This work is also supported by BK21 project corp.

References

[1] K.M. Batoo, S. Kumar, R. Prakash, Alimuddin, I. Song, H. Chung, H. Jeong, C.G. Lee, J. Cent. South Univ. Technol. 17 (2010) 1129–1132.
[2] S. Kumar, A.M.M. Farea, K.M. Batoo, C.G. Lee, B.H. Koo, A. Yousef, Alimuddin, Physica B 403 (2008) 3604–3607.
[3] K.M. Batoo, S. Kumar, C.G. Lee, Alimuddin, J. Alloy Compd. 480 (2009) 596–602.
[4] E.M. Mohammed, Plast. Rubber Compos. 3 (2002) 31.
[5] S. Kumar, S.K. Sharma, Alimuddin, M. Knobel, R.J. Choudhary, C.G. Lee, B.H. Koo, R. Kumar, Curr. Appl. Phys. 9 (2009) 1009–1013.
[6] J. Smit, H.P.G. Wijn, Ferrites (1959) 136–175.
[7] S. Kumar, R. Kumar, P. Thakur, K.H. Chae, S.K. Sharma, Alimuddin, J. Magn. Magn. Mater. 320 (2008) e121–e124.
[8] M. Sugimoto, Ceram. J. Am. Soc. 82 (2) (1999) 269–279.
[9] S. Kumar, K.M. Batoo, R. Prakash, Alimuddin, H.K. Choi, B.H. Koo, J.I. Song, H. Chung, H. Jeong, C.G. Lee, J. Cent. South Univ. Technol. 17 (2010) 1133–1138.
[10] Y. Yamamoto, Makino, J. Magn. Magn. Mater. 133 (1994) 500–503.
[11] K.M. Batoo, S. Kumar, C.G. Lee, Alimuddin, Curr. Appl. Phys. 9 (2009) 1397–1406.
[12] A.M.M. Farea, S. Kumar, K.M. Batoo, A. Yousef, C.G. Lee, Alimuddin, J. Alloy Compd. 469 (2009) 451.
[13] K.M. Batoo, S. Kumar, C.G. Lee, Alimuddin, J. Alloy Compd. 480 (2009) 596–602.
[14] S. Kumar, Alimuddin, R. Kumar, A. Dogra, V.R. Reddy, A. Banerjee, J. Appl. Phys. 99 (2006) 08M910.
[15] V. Verma, M.A. Dar, V. Pandey, A. Singh, S. Annapoorni, R.K. Kotnala, Mater. Chem. Phys. 122 (2010) 133.
[16] A.A. Satar, H.M. El-Sayed, K.M. El-Shokrofy, M.M. El-Tabey, J. Appl. Sci. 5 (1) (2005) 162–168.
[17] P. Chandra, J. Mater. Sci. Lett. 6 (1987) 651–652.
[18] R. Laishram, S. Phanjoubam, H.N.K. Sarma, C. Prakash, J. Phys. D: Appl. Phys. 32 (1999) 2151.
[19] M. Chanda, Science of Engineering Materials, vol. 3, The Macmillan Company of India Ltd., New Delhi, 1980.
[20] J.C. Maxwell, Electricity and Magnetism, vol. 1, Oxford University Press, Oxford, 1929 (Section 328).
[21] K.W. Wagner, Ann. Phys. 40 (1913) 817.
[22] I.T. Rabinkin, Z.I. Novikova, Ferrites, Izv Acad. Nauk USSR Minsk, 1960.
[23] J.C. Maxwell, Electricity and Magnetism, vol. 2, Oxford University Press, New York, 1973.
[24] R.G. Kharabe, R.S. Devan, C.M. Kanamadi, B.K. Chougule, Smart Mater. Struct. 15 (2006) N36.
[25] N. Rezlescu, E. Rezlescu, Phys. Status Solidi A 59 (1980) 323.
[26] A. Verma, O.P. Thakur, C. Prakash, T.C. Goel, R.G. Mendiratta, Mater. Sci. Eng. B 116 (2005) 1.
[27] M. Pollak, Proc. Internat. Conf. on Physics of Semiconductors (Exeter, 1962), 1962, p. 86.
[28] A.M. Abo El Ata, M.K. El Nimra, S.M. Attia, D. El Kony, A.H. Al-Hammadi, J. Magn. Magn. Mater. 297 (2006) 33.
[29] S.S. Bellad, B.K. Chougule, J. Mater. Chem. Phys. 66 (2000) 58.
[30] J.E. Bauerle, J. Phys. Chem. Solids 30 (1969) 2657.
[31] P. Knauth, L.H. Tuller, J. Am. Ceram. Soc. 85 (7) (2002) 1654.
[32] J.T.S. Irvine, D.C. Sinclair, A.R. West, Adv. Mater. 2–3 (2004) 132–138.
[33] S. Kumar, R. Prakash, Alimuddin, H.K. Choi, B.H. Koo, J.I. Song, H. Chung, H. Jeong, C.G. lee, J. Cent. South Univ. Technol. 17 (2010) 1139–1143.
[34] P.S. Anil Kumar, J.J. Shrotri, S.D. Kulkarni, C.E. Deshpande, S.K. Date, Mater. Lett. 27 (1996) 223.
[35] S. Kumar, Alimuddin, P. Kumar, K.H. Thakur, B. Chae, W.K. Angadi, J. Choi, Phys.: Condens. Matter 19 (2007) 476210.